

Multiphysics Simulation of Magnetically Actuated Robotic Origami Worms

Ruphan Swaminathan , Catherine Jiayi Cai, Sishen Yuan , and Hongliang Ren , *Senior Member, IEEE*

Abstract—Multiphysics simulation of magnetically actuated origami robots promises a range of applications such as synthetic data generation, design parameter optimization, predicting the robot's performance, and implementing various control algorithms, but it has rarely been explored. This letter presents a realistic multiphysics simulation of magnetically actuated origami robots with focus on real-time interactions between the origami and magnets. Due to the interaction between multiple magnets, the complex motion dynamics of a worm-like robot are generated and analyzed. We further show the possibility of accurately simulating origami structures made of different materials and permanent magnets of different shapes, sizes, and magnetic strength. The simulation's unknown parameters are determined by conducting similar practical and simulated experiments and comparing their characteristics. Further, we show the close resemblance between the real and simulated behavior of the origami robot.

Index Terms—Biologically-inspired robots, simulation and animation, flexible robotics.

I. INTRODUCTION

ORIGAMI is an art of letter folding and was initially introduced as a form of art. The underlying principles of origami have been applied to suit the needs of various engineering applications [1]–[4], ranging from packaging in manufacturing industries to foldable solar panels in satellites. In particular, origami concepts have a vast potential in robotics as sophisticated 3D mechanisms can be developed from 2D sheets [5], [6], giving rise to origami-inspired robots with versatile functionalities. Due to their compatibility with established 2D

fabrication techniques, the design and fabrication of robotic structures can have the potential to be inexpensive, fast, and precise. By incorporating internal permanent magnets (IPMs) into the origami robot structure, the robot can be remotely magnetically actuated via an external permanent magnetic field [10]. As magnetic actuation does not require an on-board power source, the origami robot can be compact and lightweight. These factors make them suitable for biomedical applications, such as drug injection and minimally invasive surgeries [7]–[9].

The existing literature has commonly employed electromagnetic coils or permanent magnets to generate an external magnetic field to control the magnetically responsive robots. Due to their finer control and their ability to rapidly control the field strength and direction to enable high-frequency field modulation, electromagnetic coils are often the preferred choice [11]. However, they are bulky, expensive, have high energy consumption, and prone to heating [12]. As a cheaper and more compact alternative, an external permanent magnet (EPM) can be employed. A varying external magnetic field can be induced by varying the EPM's location and orientation with respect to the IPMs located on the origami robot, generating torques and forces on the robot to induce motion. However, as the generated magnetic field is less uniform than that of electromagnetic coils, the actuation is significantly more complex and, as a result, often limits the number of motions that can be generated [13]. In our previous work, we have circumvented this by integrating multiple IPMs into the robot structure to give rise to complex motions due to the simultaneous and superpositioning of the forces and torques on the target [14]. However, this can further complicate the design and fabrication procedure due to the complexities associated with modeling and controlling EPM. Hence, it is essential to simulate the system to predict its performance under various conditions. It can also help us analyze the feasibility of the model and optimize various design parameters including the size, pose of IPMs and the origami crease patterns and beforehand.

The multiphysics simulation of origami worm robots under consideration involves solving multiple goals, such as the interactions between the IPMs and EPM, origami geometry, kinematics, dynamics, and each crease's folding in the presence of multiple constraints simultaneously. This research problem has rarely been explored as a whole in a single simulation setup. To address this gap in this letter, we present a multiphysics simulation of the origami worm robot fabricated in our previous work. All the simulations performed are done using Grasshopper 3D, a visual programming environment in Rhinoceros 3D. Kangaroo, a Grasshopper 3D plug-in, is used to set practical constraints and iteratively simulate the system. Kangaroo simulations are nonlinear [15], making them ideal for worm-like origami simulations, which tend to have large deformations from

Manuscript received October 15, 2020; accepted February 13, 2021. Date of publication March 24, 2021; date of current version April 19, 2021. This letter was recommended for publication by Associate Editor J. Rosell and Editor N. Amato upon evaluation of the reviewer's comments. This work was supported by the Chinese University of Hong Kong (CUHK) Direct Grant 4055139 for the project on Multiphysics Study of Magnetically Deployable Robotic Collapsible Structures. (Corresponding author: Hongliang Ren.)

Ruphan Swaminathan is with the Department of Electronic Engineering, Chinese University of Hong Kong, Hong Kong, and Department of Electrical and Electronics Engineering, National Institute of Technology Tiruchirappalli, Tamil Nadu 638052, India (e-mail: ruphan@live.in).

Catherine Jiayi Cai is with the Department of Biomedical Engineering, National University of Singapore, and Singapore Institute of Manufacturing Technology, Singapore 579819, Singapore (e-mail: caijiayi96@gmail.com).

Sishen Yuan is with the Department of Electronic Engineering, Chinese University of Hong Kong, Hong Kong, and the School of Mechanical Engineering and Automation, Harbin Institute of Technology, Shenzhen 518000, China (e-mail: 18s053175@stu.hit.edu.cn).

Hongliang Ren is with the Department of Electronic Engineering, Chinese University of Hong Kong, Hong Kong, and the Department of Biomedical Engineering, National University of Singapore, Singapore (e-mail: hlren@ieee.org).

This article has supplementary downloadable material available at <https://doi.org/10.1109/LRA.2021.3068707>, provided by the authors.

Digital Object Identifier 10.1109/LRA.2021.3068707

the initial state. The solver of the first version of Kangaroo was implemented using a variational form of the implicit Euler method. The current version uses projective constraint-based solving, similar to Shape-Up [16], a general-purpose simulation tool. A similar process of origami modeling has been done for the Miura pattern [17], and the authors show the feasibility of the algorithms compiled in Grasshopper 3D. Apart from predicting robotic origami structure's performance, a realistic simulation has other advantages: exploring design parameter space exhaustively and generating huge datasets for training artificial neural networks, typically costly for realistic robotic experiments. Since a magnetically actuated origami robot is an open-loop control system, it is necessary to obtain closed-loop control feedback. One way to obtain this in real-time is by using a camera to capture origami structure, which can be used as an input to a deep learning neural network to estimate the origami's configuration. In such cases, obtaining real datasets becomes an exhausting task due to the amount of data and labeling required. Deep learning models can be trained on a simulated dataset and transferred to work on real data using techniques such as domain adaptation and randomization [18]–[20] with minimal manual dataset collection. This letter contributes (1) Realistic multiphysics simulations of magnetically actuated origami worm robots in Grasshopper3D; (2) Real-time simulation and interaction with the origami and magnets; (3) Facilitate implicit setting of the type of material of the origami; (4) Generation and analysis of complex robot mechanics, kinematics and dynamics.

II. MAGNET SIMULATOR

It is essential to accurately simulate the interaction between multiple magnets in real-time to obtain a realistic simulation of the origami motion. This study adopts a magnetic model that assumes that a magnetized object is an aggregation of tiny magnetic dipoles evenly spread across the object's volume.

A. Point Magnetic Charge Dipole Model

In contrast to electric charges, the presence of magnetic charges (monopoles) has not been observed. However, modeling magnetic dipoles similar to electrical dipoles by assuming the presence of fictitious magnetic charges is a good approximation [21]. Other methods, such as circulating current loops to model a magnetic dipole, tend to be computationally intensive, making them unsuitable for real-time simulations. The model of a magnetic dipole in this study consists of equal and opposite point magnetic charges separated by a distance, d , as illustrated in Fig. 1(a). The red and blue dots represent the positive (magnetic north) and negative (magnetic south) magnetic charges. The magnetic dipole moment, m , is computed similar to that of an electric dipole, as shown in eq. (1), where the direction of m and d point from the south to the north pole. The positional vector of the center of the dipole with respect to the reference (O) is denoted by \vec{r} .

$$\vec{m} = q_m \vec{d} \quad (1)$$

Analogous to an electric dipole, the force between two monopoles is calculated using the inverse square law. Fig. 1(b) depicts the interaction between two dipoles M1 and M2. For n such dipoles, the net force acting on the i_{th} north/south

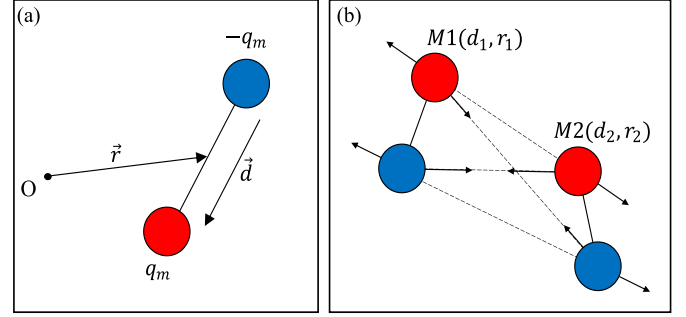


Fig. 1. Point magnetic charge dipole model. (a) A magnetic dipole modeled as a pair of oppositely charged monopoles. (b) Interaction between two magnetic dipoles, M1 and M2 (the directional and positional vectors are given inside the brackets). The arrows denote the force acting on each monopole.

monopole is

$$\begin{aligned} \vec{F}_{\left(\frac{N}{S}\right)}(i, n) = & \sum_{\substack{1 \leq j \leq n \\ j \neq i}} \frac{\mu_0 q_{mi} q_{mj}}{4\pi \left\| \vec{r}_{ij} \pm \frac{\vec{d}_{ij}}{2} \right\|^2} \left(\hat{r}_{ij} \pm \frac{\hat{d}_{ij}}{2} \right) \\ & - \frac{\mu_0 q_{mi} q_{mj}}{4\pi \left\| \vec{r}_{ij} \pm \frac{\vec{d}_i + \vec{d}_j}{2} \right\|^2} \left(\hat{r}_{ij} \pm \frac{\hat{d}_i + \hat{d}_j}{2} \right) \end{aligned} \quad (2)$$

where the positive and negative signs correspond to the north (N) and south (S) poles, respectively. The vector, $\vec{v}_{ij} = \vec{v}_i - \vec{v}_j$ and \hat{v}_i is the unit vector of \vec{v}_i , where \vec{v} can be \vec{r} or \vec{d} . It can be seen that the force caused by the other monopole of the i_{th} dipole is not accounted for, as the magnets are considered to be rigid bodies with no net internal force. To model the dipole as a single entity, the north and south monopoles are connected through a rigid beam, using the *Length* component in Grasshopper3D. This keeps the north and south monopoles of dipole always separated by a constant distance, which is mathematically represented in eq. (3). As the monopoles are connected, the forces acting on them give rise to a net force and torque acting on the dipole. The net force and torque acting on the i_{th} dipole due to remaining dipoles is shown in eq. (4) and (5), respectively.

$$\Delta \parallel \vec{d}_i \left(\vec{r}_i, t \right) = 0 \quad (3)$$

$$\vec{F}(i, n) = \vec{F}_N(i, n) + \vec{F}_S(i, n) \quad (4)$$

$$\vec{\tau}(i, n) = \frac{\vec{d}_i}{2} \otimes \vec{F}_N(i, n) - \frac{\vec{d}_i}{2} \otimes \vec{F}_S(i, n) \quad (5)$$

where \otimes denotes vector product.

B. Simulating Bar and Disk Magnets

While magnetic dipoles can be modeled as a pair of oppositely charged point magnetic charges, real permanent magnets are more complex. They are made up of uniformly distributed microscopic magnetic dipoles aligned in the same direction. The study in [22] shows that any homogeneously magnetized permanent magnet can be decomposed into an aggregation of tiny magnetic dipoles distributed throughout the object uniformly.

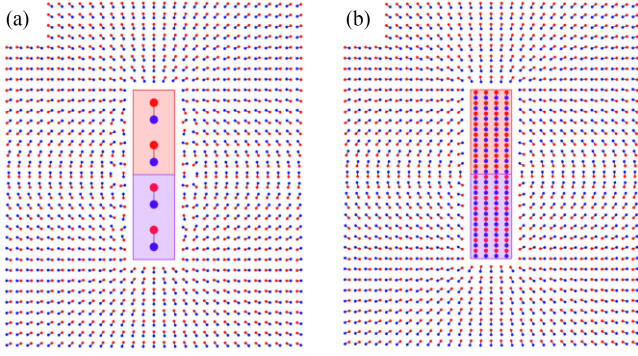


Fig. 2. Magnetic field around the two bar magnet models designed as an aggregation of magnetic dipoles. (a) Dipole density = 1 per cm^3 , (b) Dipole density = 64 per cm^3 .

The interaction between such magnets is computed by the vector sum of all the possible dipole pair interactions. The study also shows that by increasing the dipole's density, the simulated and real values of the force between two homogeneously magnetized bar magnets converge. However, very high dipole densities can become computationally intensive, and an optimal value needs to be chosen according to the simulation's requirements. This study uses a dipole density of 64 per cm^3 (as shown in section IV, Part A) since all the magnets are at least 5 mm apart from each other in our origami setup. The two-dimensional view of two different models of bar magnets with length = 1 cm, breadth = 1 cm, and height = 4 cm is illustrated in Fig. 2. The bar magnets are surrounded by dipoles anchored at their centers to visualize the magnetic field, allowing free rotation. It can be seen clearly that the field closer to the bar magnet in Fig. 2(b) is much better than that in Fig. 2(a).

The EPM is modeled as a bar magnet, and the IPMs are modeled as disk magnets with dipoles aligned in the same direction and evenly spread throughout the magnet. Further, to make all the dipoles in a magnet as a single entity, the *RigidBody* component in Grasshopper3D is used. The net force and torque experienced by an IPM are calculated as the vector sum of the individual forces and torques experienced by each dipole in the magnet as described in eq. (4) and (5).

III. ORIGAMI DESIGN AND STEERING

In general, origami robot design and simulations [23]–[25] assume rigid facets due to their negligible bending and reduced computational complexity. Thus, even though the individual triangular facets are rigid, the mesh is overall a non-rigid body due to the foldability at the creases. Similar to the mesh facets being modeled as rigid panels to avoid bending, all the mesh edges, which includes the creases, are modeled as rigid beams to avoid stretching of the letter. The creases are also modeled as revolute joints that connect two triangular facets. The crease lines belong either to a mountain fold or a valley fold whose folding angle lies in the range of 0 to $-\pi$ or 0 to π , respectively. The folding angle of a crease refers to the angle between the planes of panels adjoining it. Hence the folding angles of all the creases are zero in a flat sheet of letter. The worm robot is a triangular tessellation in which the elementary unit repeats to form the pattern. This elementary unit is constructed as a mesh in Grasshopper 3D, shaped like a triangular prism, as shown in Fig. 3. To construct the complete origami, n_o such units are

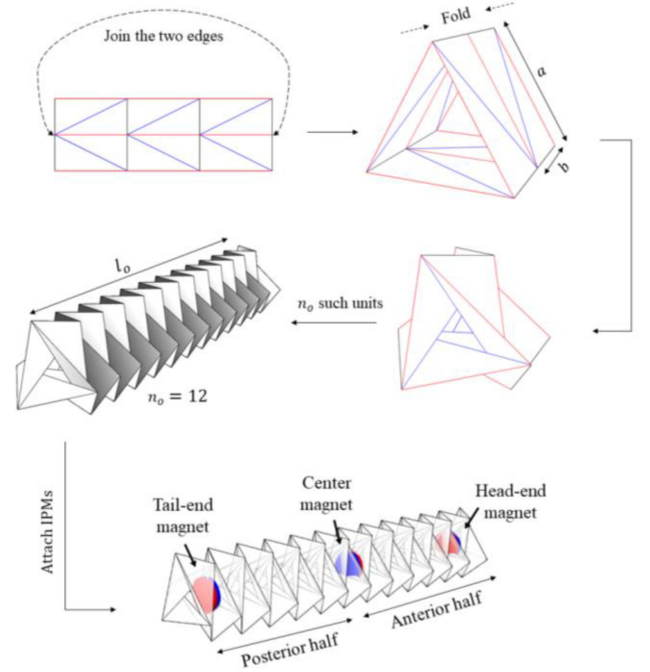


Fig. 3. Construction of the worm origami robot. The red lines denote the valley folds, and the blue lines denote the mountain folds. The parameters a , b and n are chosen according to the simulation's requirements.

joined together. At equilibrium, in the absence of external forces and magnetic fields, the folding angles of all the mountain and valley folds are $-\alpha$ and α , respectively ($\alpha \in [0, \pi]$) due to the inherent symmetry of the origami structure. The value of α depends on the crease stiffness of the material used in making the origami and can be determined by measuring the length of the letter used and the origami's length at rest. Using the cosine rule, the relation between the origami's length (l_o) and α can be computed as

$$\left(\frac{l_o}{n_o}\right)^2 = (b)^2 + (b)^2 + 2(b)(b)\cos(\pi - \alpha) \quad (6)$$

Thus, the initial folding angle ($-\alpha$ and α , for mountain and valley folds, respectively) for all the folds can be expressed as

$$\alpha = \pi - \cos^{-1}\left(1 - \frac{l_o^2}{2n_o^2b^2}\right) \quad (7)$$

The origami is divided into two equal sections – the anterior and the posterior half, to attach the magnets in the origami for suitable actuation. The IPMs are embedded in the three junction points, the tail end, the center, and the head end. The orientation of the magnets is illustrated in Fig. 3. Kangaroo is an interactive physics engine that is used to achieve the goals set by iterative solving. The components of this plug-in are used to set the suitable goals and constraints of the simulation. Creases have a property called spring back or crease recovery, enabling the robot to deform in the presence of an external force and bounce back to its original state, like an angular spring. To mimic this behavior, all the revolute joints are modeled using the *Hinge* component in Grasshopper 3D and assigned with a strength parameter k_α which tries to maintain the value of α . The relation between α , k_α , and the external forces acting on the hinge are governed by the equations in [26]. A higher value

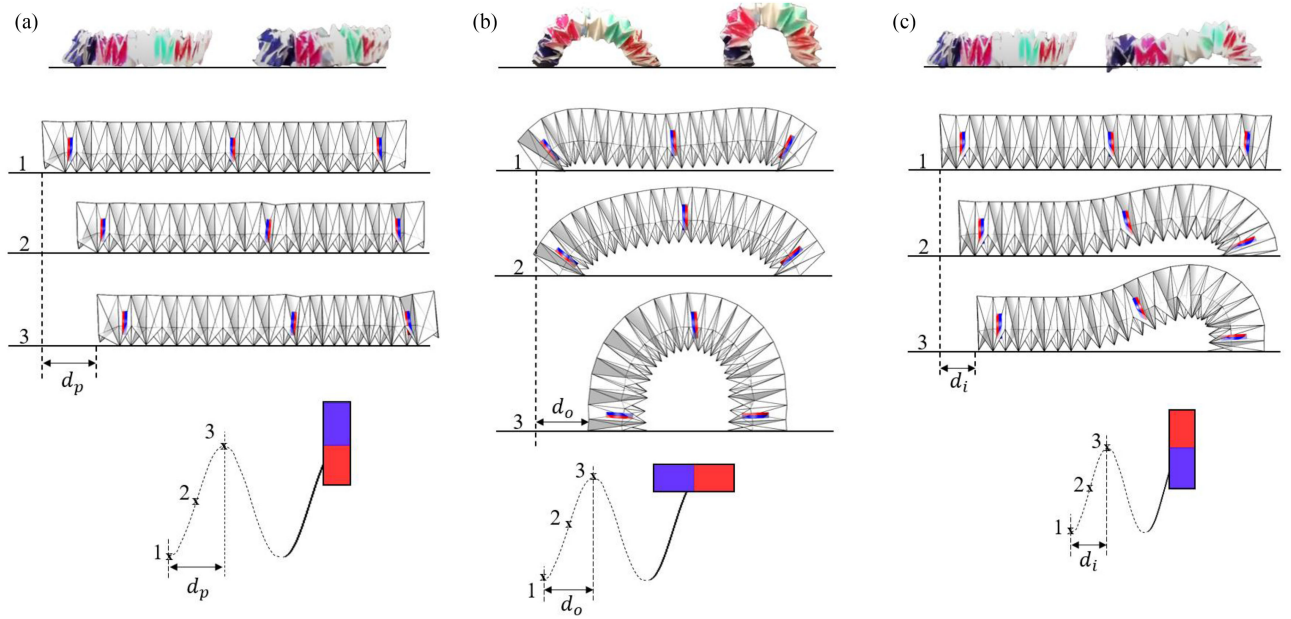


Fig. 4. Generation of different translational motions using by varying the EPM's orientation and trajectory in the Grasshopper3D. The experimental versions are shown on top of the corresponding origami motions. (a) Peristaltic motion, (b) Omega motion, (c) Inchworm motion.

of k_α makes the origami completely rigid, while a lower value makes the joints to rotate freely. Rigid beams are also used to firmly attach the IPMs with the origami mesh in the desired orientation, which allows the IPMs to deform the origami structure by transferring the force and torque applied to them by the EPM. The *Length* component is used to create rigid beams. The strength parameter of this component determines the elasticity of the beam. Setting a high value corresponds to a rigid beam (with negligible extension or compression), and a low value corresponds to linear spring-like characteristics. The constraint to avoid the individual triangular facets passing through each other is achieved by using the *NoFoldThrough* component at all the creases. The *Load* and *Floor* components provide suitable gravitational and normal forces on the origami mesh. This letter analyzes three different translational motions of the origami, namely Peristaltic, Omega, and Inchworm motions, as shown in Fig. 4. Similar to the previous work, we positioned three IPMs to the anterior, middle, and posterior end of the origami worm. However, we chose to orientate the IPMs differently and demonstrated that similar motions could be recreated with this different pattern, demonstrating the simulation's potential for origami modeling.

A. Peristaltic Motion

Peristaltic motion is a one-dimensional translation motion of the origami, similar to the contraction and relaxation behavior observed during muscle's peristalsis. The origami's contraction is due to the attractive forces between the two north poles of the IPMs in the anterior half of the origami with the south pole of the EPM. This contraction happens only in the origami's anterior region, and the posterior region retains its shape. When the EPM is moved sufficiently far away, the stiffness in the creases of the origami pushes it back to its original shape, creating a relaxation motion. The EPM is positioned a little closer to the IPM in the center, facilitating forward propagation. The same motion in the

backward direction can be achieved by bringing the north pole of an EPM between the south poles of the IPMs in the posterior half of the origami.

B. Omega Motion

The origami motion resembles the Greek alphabet omega during the motion and hence the name. The EPM is held flat with its north pole pointing forward and brought closer to the origami so that the center of the origami and the center EPM align. This configuration creates a clockwise torque on the head end IPM and an anticlockwise torque on the tail end IPM. The IPM in the middle experiences negligible torque since the clockwise and anticlockwise components almost cancel each other. However, this section is lifted upward by the magnetic force and the bending moment at the structure's ends. As the EPM is brought closer, the force of attraction between the EPM and IPMs on the extreme end and the force of repulsion between the EPM and IPM in the center increases. This configuration pushes the middle of the origami upward and brings the origami's ends closer, thus increasing the origami's curvature. The EPM is also moved in the forward direction simultaneously, which helps in the origami's forward translational motion. The omega motion is two-dimensional and utilizes a larger space. Despite this, it is suitable for locomotion in rough terrain where lesser surface contact is desirable.

C. Inchworm Motion

The inchworm motion is a combination of peristaltic and omega motion. The north pole of the EPM is brought between the north poles of the IPMs in the origami's anterior half. This configuration creates a clockwise torque on the front end IPM and an anticlockwise torque on the center IPM, similar to that in the omega motion. Hence it allows the origami's anterior region to take the shape of omega while the posterior region

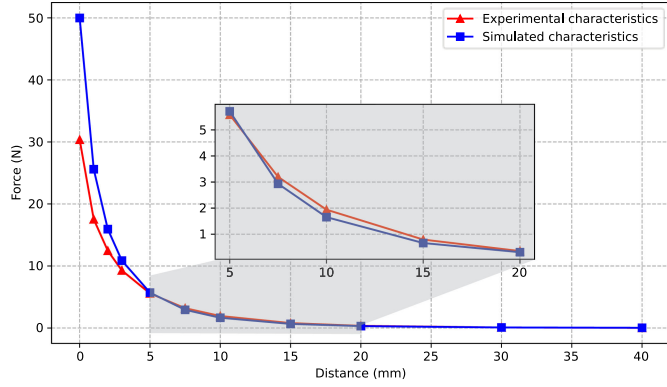


Fig. 5. The attractive force between two magnets (unlike poles facing each other) in the Grasshopper3D environment and the experimental setup. The close resemblance between simulated and real behavior in the origami's operating range is shown as a magnified view in the inset, where the distance between the magnets is at least 5 mm.

maintains its shape. Like the peristaltic motion, the EPM is closer to the IPM in the center to facilitate the origami's forward translational motion. The IPM in the center plays a vital role during this motion. The anticlockwise torque acting on it creates an inverted U-shape in the anterior half and pulls the posterior half in the forward direction. Bringing the south pole of the EPM between the south poles of the IPMs in the posterior half causes the origami to move in the opposite direction. Despite being slowest, it is preferred for climbing inclined and viscous surfaces due to its higher contact friction.

IV. EXPERIMENTAL RESULTS AND VALIDATION

A. Setting Magnet Strength

The interactions between the EPM and IPMs are modeled according to the equations in section II. However, the magnetic charge (q_m) and the distance between the point magnetic charges (d) is unknown. The force-distance characteristic of two N52 grade neodymium cube magnets (volume = 1 cm^3) with the unlike poles facing each other is determined. The same setup is simulated in the Grasshopper3D environment to fix the unknown parameters by fitting the simulated force-distance characteristics with the real one. Interestingly, it was found that for a constant dipole moment and d size of the magnet, the value of d had a negligible effect on the force between the magnets. It is to be noted here that, due to the alignment of the dipoles in the same direction, the magnitude of the dipole moment of the magnet is the sum of the magnitudes of individual dipoles in the magnet. Thus, we arbitrarily fix the value of d as $1 \mu\text{m}$ and the dipole moment of the magnet is varied to fit the force-distance characteristics. For a dipole moment of 0.9 Am^2 and a dipole density of 64 per cm^3 , the simulated and experimental characteristics match closely in the magnet's operating range, as shown in Fig. 5. The EPM is a cuboid of size, $10 \text{ mm} \times 10 \text{ mm} \times 40 \text{ mm}$, and the IPMs are disk magnets with a diameter and thickness of 10 mm and 1 mm , respectively. Thus, with a dipole density of $64/\text{cm}^3$, a total of 271 dipoles are present. The time complexity of the dipole interactions is $O(N^2)$, as observed in eq. (2). The simulation of the interactions was carried out on an Intel Core i7-8550U CPU. The Kangaroo solver performed ~ 400 iterations per second, thus facilitating real-time implementation and interaction with the simulation.

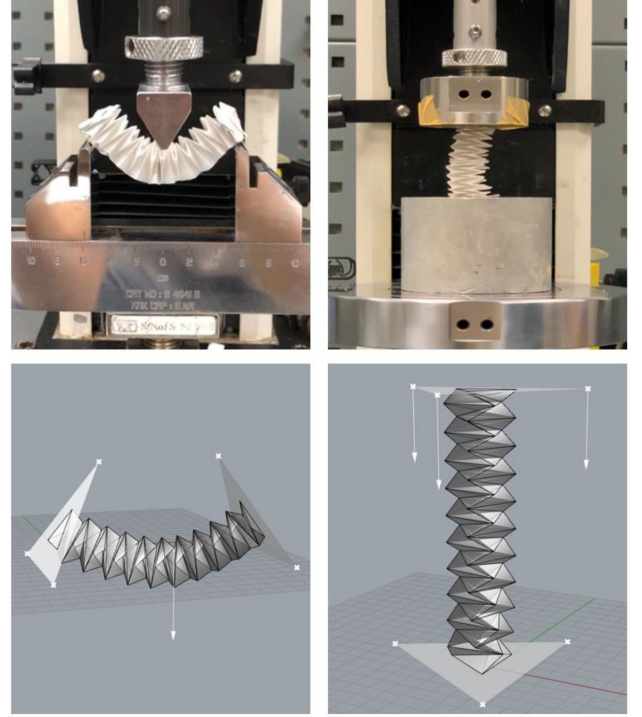


Fig. 6. Test environment to perform the compression and 3-point flexure test in the experimental (top) environment. The same test is employed on the simulated origami structure (bottom) to determine the *Hinge* component's strength parameter.

B. Simulating Origami Made of Different Materials

The nature of the creases varies based on the type of material used to make the origami robot. The folding angle of the origami, which depends on the crease stiffness, can be determined by physically measuring the origami robot's length using eq. (7). As shown in Fig. 6, an experimental and simulated setup is used to perform the compression and 3-point flexure test on the origami. In the experimental setup, three origami structures are built using different materials, and the resultant characteristics are illustrated as solid lines in Fig. 7(a), (b), (c). In the simulation setup, the value of the strength parameter (k_α) of the *Hinge* component is tuned to match the experimental characteristics. The effectiveness of such a method to implicitly set the type of material by varying the hinge parameter's strength can be seen in Fig. 7(d). Despite the entirely different nature of the compression and 3-point flexure tests, the obtained value of k_α from both tests are very close for all the three materials. The average value of k_α obtained from the compression and 3-point flexure test is used as the final value for the Hinge component's strength parameter.

C. The Trajectory of the EPM

The motion of the EPM determines the motion of the origami. The parameters defining the motion of the EPM are wavelength (w), amplitude (a), closest approach from the origami base (h), and the orientation of the magnet (θ), as shown in Fig. 8. The significance of each parameter is as follows:

- 1) The wavelength of the sinusoidal motion determines the distance covered by the origami in one cycle. A smaller

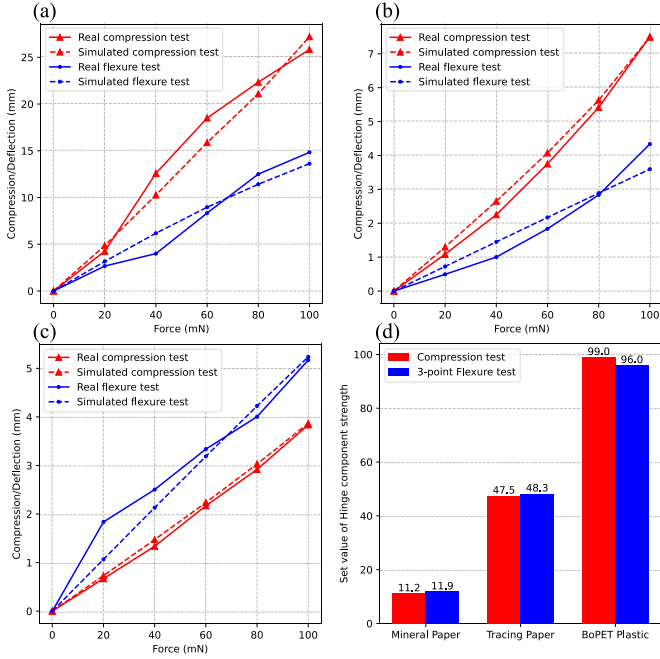


Fig. 7. Setting the *Hinge* component's strength in Grasshopper3D by performing compression and 3-point flexure test in an experimental and simulated environment. (a) Characteristics of mineral paper, (b) Characteristics of tracing paper, (c) Characteristics of BoPET plastic, (d) Comparison of the set value of strength for different materials between the compression and 3-point flexure test in Grasshopper3D environment.

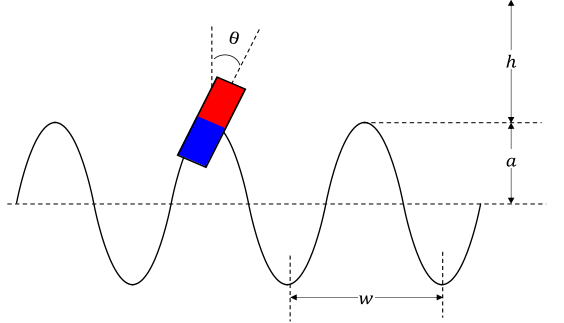


Fig. 8. The four parameters that define the orientation and trajectory of the EPM to produce different origami dynamics.

wavelength restricts the origami speed, while a large wavelength makes it difficult for the origami to keep up.

- 2) The amplitude of the sine wave determines the maximum distance of the origami from the magnet, which should be sufficiently large to avoid any movement in the origami.
- 3) The closest approach indirectly determines the amount of energy transferred to the origami, and a very small value tends to crumple the origami. Thus it dictates the maximum magnetic flux density in the origami base.
- 4) The orientation of the EPM decides the type of motion based on the torques acting on the IPM.

The orientation of the EPM can be intuitively determined based on the type of motion required. However, the other three parameters are identified using a grid search algorithm to maximize the distance that the origami moves. The obtained optimal values of the parameters are listed in Tab. I.

TABLE I
THE CHARACTERISTICS OF THE SINUSOIDAL MAGNETIC MOTION TO ACHIEVE DIFFERENT ORIGAMI MOTIONS

Motion/Characteristic	Peristalsis	Inchworm	Omega
Wavelength (mm)	8.5	6	7.5
Amplitude (mm)	10	6	8
Closest approach (mm)	9	11	5
Orientation (degrees)	180°	0°	90°

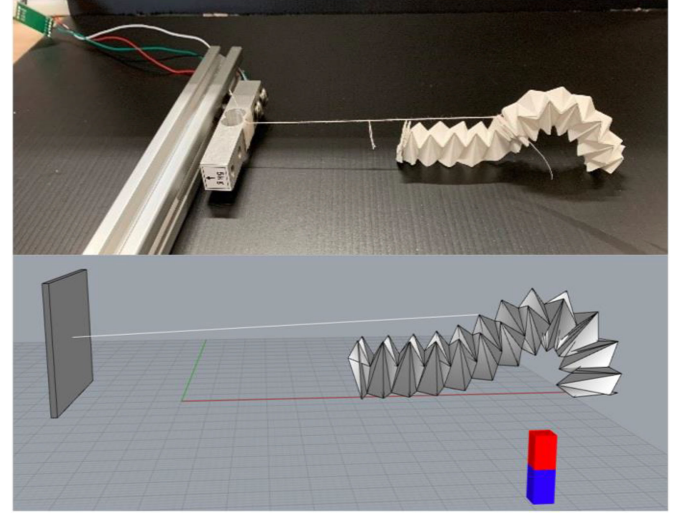


Fig. 9. Measuring the force exerted by origami (inchworm motion) in the experimental (top) and simulation environment (bottom).

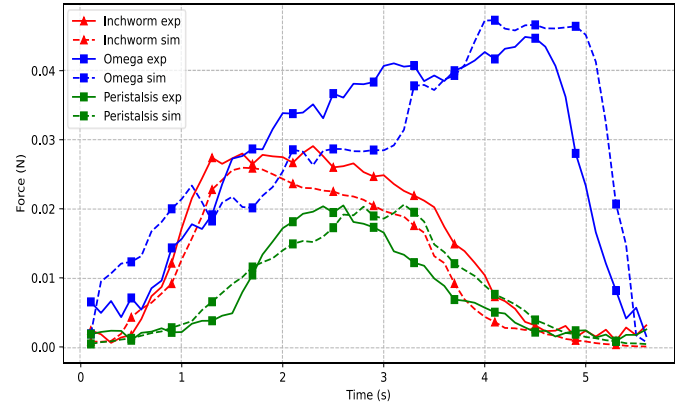


Fig. 10. Comparison between the force exerted by different origami motions in the experimental (solid lines) and the simulation (dashed lines) setup.

D. Force Analysis

One of the origami robot's vital functions is to move objects by exerting a force on them. For example, an origami robot used in minimally invasive surgeries needs to push/pull polyps and tissues. Hence it is necessary to predict the characteristics of the dynamic force exerted by the origami during various motions. Fig. 9 shows the experimental and simulated setup of the origami exerting a pulling force during inchworm motion. One end of a string is tied to the origami, and the other is

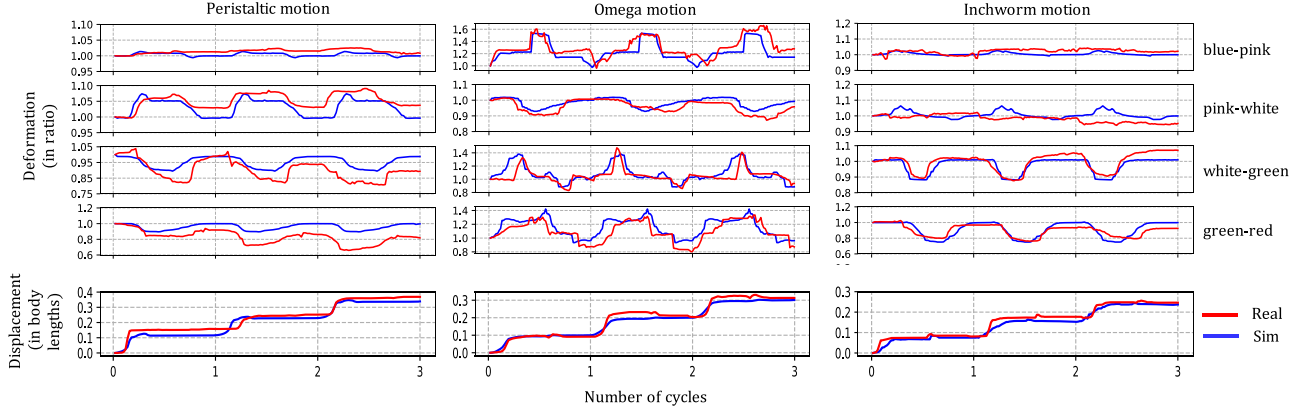


Fig. 11. Quantitative analysis of deformation and displacement of the different origami gaits in real (red) and simulation (blue). The three rows correspond to the three different gaits: Peristaltic, Omega, and Inchworm motions (in row-wise order). The deformation ratio corresponds to the shrink/expansion of the particular segment of the origami during its motion.

fixed to the force plate. In the simulation, the string is fixed to the force plate using the *Anchor* component with high strength (in the order of 10^4). The experiment was done using mineral letter. Thus, in the simulation, the hinge strength (k_α) is set as 11.55. Conventionally, the force measurement is done by multiplying the strength parameter of the *Anchor* component with the displacement vector of the fixed point. The variation of force with respect to time for three different motions (Inchworm, Peristaltic, and Omega) in the simulation and the experimental setup is plotted in Fig. 10. The characteristics of the force curves in the experimental setup, such as a steep rise and a smooth fall for the inchworm motion and vice versa for the omega motion, resemble the force curves of the experimental setup.

E. Deformation and Displacement Analysis

Fig. 11 shows a quantitative comparison between the real and simulation experiments to determine the deformation and displacement behavior of the different origami motions. To track the origami's deformation throughout its motion, five equally spaced key points are chosen, and the distance between them is measured. In the real experiment, the origami is divided into five equal segments and colored with blue, pink, white, green, and red (in order from the posterior end). The distances between the adjacent segment's centers are tracked, giving rise to four different deformation values (blue-pink, pink-white, white-green, and green-red) at every instance. For ease of analysis, the deformation values are normalized by dividing them by the initial deformation values. Thus, a deformation value lesser than 1 and greater than 1 corresponds to compression and expansion of the corresponding segments, respectively. The visible deviation between real and simulated deformation, as seen in the green-red deformation of peristalsis, is due to the plasticity of letter crease folds. The real origami tends to not fully recover to its initial state after continuous deformations due to the hysteresis of crease plasticity [27]. In contrast, the simulated origami resembles an ideal spring that returns to its natural state after removing the external magnetic field.

F. Surface Contact Model

A surface-point contact model is adopted in this study. The *Floor* component in Grasshopper opposes the origami's weight

by exerting a normal force at each contact point with the surface. These contact points are projected slightly below the xy-plane. Thus the contact points (P_c) are determined by sorting the origami mesh vertices based on their z-coordinates and choosing the vertices that lie below the xy-plane. The projected z-coordinates of the contact points are multiplied with the *Floor* component's strength parameter to obtain the normal forces (\vec{F}_n) at the contact points. Thus, even when the load distribution is uneven during different gaits, the normal forces acting on the contact points are accurately computed.

Using this, a realistic static friction model that can exert varying amounts of forces at each contact point is obtained, as expressed below

$$\vec{f}(p, t) = \min \left(\vec{F}_h(p, t), \mu \vec{F}_n(p, t) \right) \quad \forall p \in P_c \quad (8)$$

where $\vec{f}(p, t)$, $\vec{F}_h(p)$, $\vec{F}_n(p)$ represent the frictional force, horizontal force, and the normal force acting at the contact point p at time t , and μ is the coefficient of static friction. The value of μ was found to be 0.268 by performing a simple slope sliding test. At some instants (during inchworm and omega), the end faces also contact the surface. In those cases, the surface-surface friction is approximated as surface-point friction as the first-order approximation of static friction is independent of contact area [28].

G. Strain Analysis

It is essential to know the strain induced in the origami during different locomotion gaits to ensure that the material used for making the origami lasts long. The origami's valley and mountain folds are made with beams of high rigidity to prevent the letter from crumpling. During different locomotion gaits, these beams experience a compressive or expansion force. Continuous application of such forces may cause wear and tear of the material used in making the origami. Thus, it is vital to analyze the dynamic strain on the origami. Cauchy strain (dimensionless quantity) is used for this purpose, which is computed and visualized by using a gradient that varies from blue (no strain) to red (maximum strain), as shown in Fig. 12.

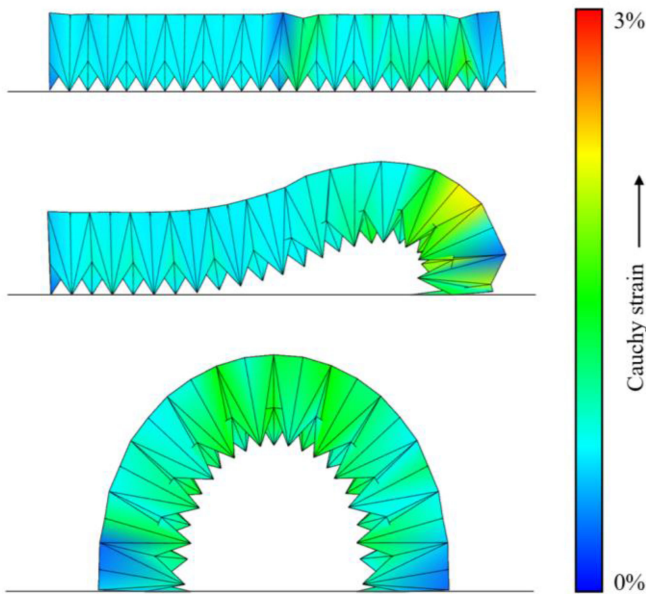


Fig. 12. Cauchy strain experienced by the origami during different motions is visualized by using a color gradient from blue (no strain) to red (maximum strain).

V. CONCLUSION

This letter presents multiphysics simulation of a magnetically actuated origami robot using Grasshopper3D. The origami robot is embedded with multiple IPMs, and an external magnetic driving field generated by EPM is used to actuate and control the robot. A realistic simulation was achieved using Kangaroo, the physics engine plug-in of Grasshopper3D. Practical experiments further determined the unknown parameters of the simulation and validated the simulation.

This study is the first to demonstrate a realistic simulation of magnetically actuated origami worm robots, and there is much scope for improvements in the future. A few areas that need further investigation are the hinge model, contact model and EPM trajectory analysis. Customized models could replace Kangaroo components to improve the simulation's behavior further. A control algorithm can be developed to analyze the effects of the EPM trajectory on the origami's locomotion. Our future work involves using this simulation to optimize the worm robot design and generate huge datasets to train deep learning algorithms for 6-DOF pose estimation.

ACKNOWLEDGMENT

We thank Zhang Yan and Huxin Gao for their assistance and support in the experiments.

REFERENCES

- [1] D. J. Balkcom and M. T. Mason, "Introducing robotic origami folding," in *Proc. IEEE Int. Conf. Robot. Automat.*, vol. 4, pp. 3245–3250, 2004.
- [2] H. Yang *et al.*, "Multifunctional metallic backbones for origami robotics with strain sensing and wireless communication capabilities," *Sci. Robot.*, vol. 4, no. 33, 2019.

- [3] H. Banerjee, T. K. Li, G. Ponraj, S. K. Kirthika, C. M. Lim, and H. Ren, "Origami-Layer-Jamming deployable surgical retractor with variable stiffness and tactile sensing," *J. Mechanisms Robot.*, vol. 12, no. 3, pp. 1–15, Jan. 2020.
- [4] H. Yang *et al.*, "Graphene oxide-enabled synthesis of metal oxide origamis for soft robotics," *ACS Nano*, vol. 13, no. 5, pp. 5410–5420, Mar. 2019.
- [5] C. D. Onal, R. J. Wood, and D. Rus, "Towards printable robotics: Origami-inspired planar fabrication of three-dimensional mechanisms," in *Proc. IEEE Int. Conf. Robot. Automat.*, pp. 4608–4613, 2011.
- [6] S. M. Felton, M. T. Tolley, C. D. Onal, D. Rus, and R. J. Wood, "Robot self-assembly by folding: A printed inchworm robot," in *IEEE Int. Conf. Robot. Automat.*, Karlsruhe, Germany, 2013, pp. 277–282.
- [7] A. Abramson *et al.*, "An ingestible self-orienting system for oral delivery of macromolecules," *Science*, vol. 363, no. 6427, pp. 611–615, 2019.
- [8] S. Miyashita, S. Guitron, K. Yoshida, S. Li, D. D. Damian, and D. Rus, "Ingestible, controllable, and degradable origami robot for patching stomach wounds," in *IEEE Int. Conf. Robot. Automat. (ICRA)*, 2016, pp. 909–916.
- [9] B. S. Yeow, J. Sun, J. Ho, and H. Ren, "Towards magnetically actuated Guide-wire steering in arteriovenous fistula angioplasty procedures," in *Proc. IEEE Conf. Real-time Comput. Robot. (RCAR)*, Angkor Wat, Cambodia, 2016, pp. 1–6.
- [10] S. Miyashita, S. Guitron, M. Ludersdorfer, C. R. Sung, and D. Rus, "An untethered miniature origami robot that self-folds, walks, swims, and degrades," in *Proc. IEEE Int. Conf. Robot. Automat. (ICRA)*, 2015, pp. 1490–1496.
- [11] P. Ryan and E. Diller, "Magnetic actuation for full dexterity microrobotic control using rotating permanent magnets," *IEEE Trans. Robot.*, vol. 33, no. 6, pp. 1398–1409, 2017.
- [12] G. Pittiglio *et al.*, "Magnetic levitation for soft-tethered capsule colonoscopy actuated with a single permanent magnet: A dynamic control approach," *IEEE Robot. Autom. Lett.*, vol. 4, no. 2, pp. 1224–1231, 2019.
- [13] A. W. Mahoney, D. L. Cowan, K. M. Miller, and J. J. Abbott, "Control of untethered magnetically actuated tools using a rotating permanent magnet in any position," in *Proc. IEEE Int. Conf. Robot. Automat.*, 2012, pp. 3375–3380.
- [14] C. J. Cai *et al.*, "Diversified and untethered motion generation via crease patterning from magnetically actuated caterpillar-inspired origami robot," in *IEEE/ASME Trans. Mechatronics*.
- [15] D. Piker, "Kangaroo: Form finding with computational physics," *Archit. des.*, vol. 83, no. 2, pp. 136–137, 2013.
- [16] S. Bouaziz, M. Deuss, Y. Schwartzburg, T. Weise, and M. Pauly, "Shape-up: Shaping discrete geometry with projections," *Comput. Graph. Forum*, vol. 31, no. 5, pp. 1657–1667, 2012.
- [17] M. Tsimias, A. Oliva, and M. Calvano, "Algorithmic design and analysis of architectural origami," *Nexus Netw. J.*, vol. 20, no. 1, pp. 59–73, 2018.
- [18] S. James *et al.*, "Sim-to-real via Sim-to-Sim: Data-efficient robotic grasping via randomized-to-canonical adaptation networks," in *Proc. IEEE/CVF Conf. Comput. Vis. Pattern Recognit. (CVPR)*, 2019, pp. 12627–12637.
- [19] M. Islam, V. VS, C. M. Lim, and H. Ren, "ST-MTL: Spatio-temporal multitask learning model to predict scanpath while tracking instruments in robotic surgery," *Med. Image Anal.*, vol. 67, pp. 101837, 2021.
- [20] L. Qiu, C. Li, and H. Ren, "Real-time surgical instrument tracking in robot-assisted surgery using multi-domain CNN," *Healthcare Technol. Lett.*, vol. 6, no. 6, pp. 159–164, 2019.
- [21] K. Seleznyova, M. Strugatsky, and J. Kliava, "Erratum: Modelling the magnetic dipole (2016 eur. J. Phys. 37 025203)," *Eur. J. Phys.*, vol. 37, no. 3, 2016, Art. no. 039601.
- [22] B. Thomaszewski, A. Gumann, S. Pabst, and W. Straßer, "Magnets in motion," *ACM Trans. Graph.*, vol. 27, no. 5, pp. 1–9, 2008.
- [23] H. Banerjee, N. Pusalkar, and H. Ren, "Single-Motor controlled tendon driven peristaltic soft origami robot," *J. Mechanisms Robot.*, vol. 10, no. 6, pp. 64501, Sep. 2018.
- [24] T. Tachi, "Generalization of rigid foldable quadrilateral mesh origami," *J. Int. Assoc. For Shell Spatial Structures*, vol. 50, no. 162, pp. 2287–2294, 2009.
- [25] A. J. Taylor *et al.*, "MR conditional SMA-based origami joint," *IEEE/ASME Trans. Mechatronics*, vol. 24, no. 2, pp. 883–888, Apr. 2019.
- [26] D. Piker, "K2Goals," *GitHub*, 2016. Accessed: Jan. 5, 2021. [Online]. Available: <https://github.com/Dan-Piker/K2Goals/blob/master/Hinge.cs>
- [27] J. Yang, L. Jin, J. W. Hutchinson, and Z. Suo, "Plasticity retards the formation of creases," *J. Mech. Phys. Solids*, vol. 123, pp. 305–314, 2019.
- [28] V. L. Popov, "Coulomb's law of friction," in *Contact Mechanics and Friction*. Berlin, Heidelberg: Springer, 2010, pp. 133–154.